

## TABLE OF CONTENTS

	Page
<b>1 Experimental Setup</b>	<b>1</b>
1.1 The Large Hadron Collider . . . . .	2
1.1.1 Machine Design and Layout . . . . .	3
1.1.2 Injection Chain and Bunch Structure . . . . .	6
1.1.3 The Concept of Luminosity . . . . .	9
1.1.4 Operation of the Large Hadron Collider . . . . .	10
1.2 The ATLAS Detector . . . . .	12
1.2.1 The ATLAS Coordinate System . . . . .	12
1.2.2 The Inner Detector . . . . .	14
1.2.3 Calorimeter Systems . . . . .	18
1.2.4 The Muon Spectrometer . . . . .	22
<b>Bibliography</b>	<b>28</b>

# Chapter 1

## Experimental Setup

*Nice piece of wood in that counter. Nicely planed. Like the way it curves there.*

—Leopold Bloom, in James Joyce’s *Ulysses*

The work to be described in the present thesis was done at CERN<sup>1</sup>, the particle physics laboratory located along the French-Swiss border just outside of Geneva, Switzerland. CERN is comprised of almost 18,000 personnel, of which over 13,000 are researchers in the field of experimental particle physics. It is a truly international workplace, with the personnel comprised of representatives of over 110 nationalities and who are either working directly for CERN<sup>2</sup> or for their respective home institutions — universities or national labs — located across more than 70 countries worldwide [1]. These researchers will generally work at any of the independent experiments located along the various beamlines that network throughout the CERN campus (see Fig. 1.1).

At the time of writing, there are four large experiments<sup>3</sup> taking place currently at CERN, all located along the Large Hadron Collider (LHC): ALICE [2], LHCb [3], CMS [4], and ATLAS [5]. The CMS and ATLAS detectors are general purpose detectors, with broad research programs, whereas the ALICE and LHCb detectors are specialised for the study of heavy-ion collisions and  $b$ -hadron physics, respectively.

This chapter will present a brief introduction to the workings of the LHC in Section 1.1. In Section 1.2, given that the present author is a member of the ATLAS collaboration, a detailed description of the various components that make up the ATLAS detector will be presented.

---

<sup>1</sup> The acronym CERN was historically derived from ‘Conseil européen pour la recherche nucléaire’. Nowadays, ‘CERN’ has become a standalone name for the lab itself and is currently referred to as the ‘Organisation européenne pour la recherche nucléaire’; or, in English: the ‘European Organisation for Nuclear Research.’

<sup>2</sup> Of the roughly 18,000 researchers in experimental particle physics, only about 5% are employed directly by CERN itself.

<sup>3</sup> For the most part, one can interchange the words ‘detector’ and ‘experiment’ when referencing large-scale, long-term particle physics experiments such as those that have taken place over the past few decades: the detectors tend to take on the role of representing the entire collaboration of physicists, engineers and associated personnel, as well as the entire scope of the associated research programs.

CERN's Accelerator Complex

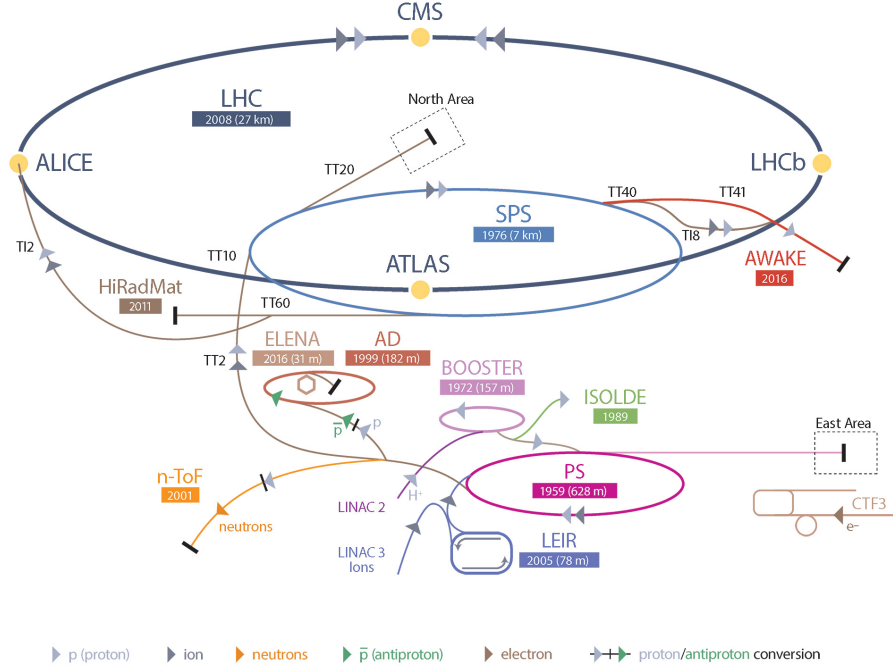


Figure 1.1: Illustration of the various beamlines, accelerator and storage rings, and experimental points that the CERN accelerator complex is home to. The protons that circulate through the LHC, and that are eventually made to collide inside the ATLAS detector, follow the path: Linac 2 → Booster → Proton Synchotron (PS) → Super Proton Synchrotron (SPS) → LHC.

## 1.1 The Large Hadron Collider

The LHC [6] is a circular particle accelerator, with a 27 kilometer circumference, located at an average distance of 100 meters beneath the surface of the Earth. It is nominally used for proton-proton ( $pp$ ) collisions, wherein two counter-rotating beams of protons are made to collide head-on at specific interaction points (IP) along the 27 kilometer ring, but can also be run in heavy-ion configurations wherein proton-lead ( $p$ -Pb) or lead-lead (Pb-Pb) collisions take place.<sup>45</sup> The  $pp$  collisions take priority over those of the heavy-ions, with the collisions each year consisting of only a few weeks in the winter for the heavy-ion configurations and typically six to seven months for the  $pp$  configuration. The LHC is designed to accelerate protons to a center-of-mass energy of  $\sqrt{s} = 14$  TeV.

<sup>4</sup>The specific lead (Pb) species used in collisions is  $^{208}\text{Pb}$ .

<sup>5</sup>More rarely, the LHC can also be used to circulate gold (Au) ions. There are even plans to have proton-oxygen ( $p$ -O) runs in the future, which will allow for the LHC experiments to provide research that potentially complements dark matter research based on cosmic-ray air showers.

### 1.1.1 Machine Design and Layout

#### Machine Composition

The LHC was planned as the successor to the Large Electron Positron (LEP) collider [7, 8], which was in operation between the years of 1989 to 2000. LEP is still the most powerful lepton collider to date, having maximal electron-positron center-of-mass collision energies of 209 GeV. After LEP, the particle physics community knew that the next collider at CERN needed to have  $\mathcal{O}(10)$  TeV collision energies; either to be able to probe from all angles any new physics discovered at LEP and/or the Tevatron [9], or to provide the necessary power to search for still-elusive hints of BSM physics. At the very least, given a non-discovery of the Higgs boson at LEP and the Tevatron, the community would need a discovery machine powerful enough to produce electroweak-scale Higgs bosons and an  $\mathcal{O}(10)$  TeV hadron collider — as we now know — is sufficient for this job.

In order to increase center-of-mass collisions energies, collider designs can take two routes: they can either increase in size, that is, have larger circumferences (radii), or they can increase the strength of the magnetic fields used to keep the circulating charged particles in orbit. This can be seen by first considering the expression for the relativistic cyclotron frequency,  $\omega$ , of a particle moving in a circular orbit,

$$\omega = \frac{qB}{\gamma m}, \quad (1.1)$$

where  $m$  is the particle's rest mass,  $B$  is the magnitude of the magnetic field experienced by the particle,  $q$  is the particle's electric charge, and  $\gamma$  is the relativistic Lorentz factor,  $\gamma = \sqrt{1 - \beta^2} = \sqrt{1 - (v/c)^2}$ , with  $v$  the particle's velocity and  $c$  the speed of light. Using Eqn. 1.1, it can be seen that a particle of higher energy confined to a fixed circular orbit necessarily has a higher angular velocity by relating the particle's angular velocity to its kinetic energy:

$$E_{\text{kin}} \propto mv^2 = m(\omega R)^2 = \frac{q^2 B^2 R^2}{m\gamma^2}. \quad (1.2)$$

In planning the construction of the LHC, the costs in civil engineering and real-estate works that would be required to construct a larger tunnel in which to house the LHC ring (increasing  $R$ ) far outweighed the costs of research into and development of magnet systems strong enough to bend the multi-TeV particles along the beam orbit prescribed by the already-existing LEP tunnel (increasing  $B$ ). The desired center-of-mass collision energy of  $\mathcal{O}(10)$  TeV, the fact that the LHC would be a hadron (proton) collider, and the fact that the LHC would be using the existing LEP tunnel dictate the required magnetic field strength needed to keep the protons in stable orbits at the LHC. This is seen by using Eqn. 1.2, solving for  $B$ , and comparing the LHC and LEP design

parameters,

$$\begin{aligned}
\frac{B_{\text{LHC}}^2}{B_{\text{LEP}}^2} &= \frac{(E_{\text{LHC}} m_{\text{LHC}} \gamma_{\text{LHC}}^2) / (q_{\text{LHC}}^2 R_{\text{LHC}}^2)}{(E_{\text{LEP}} m_{\text{LEP}} \gamma_{\text{LEP}}^2) / (q_{\text{LEP}}^2 R_{\text{LEP}}^2)} \\
&= (E_{\text{LHC}} / E_{\text{LEP}}) \times (m_{\text{LHC}} / m_{\text{LEP}}) \times (\gamma_{\text{LHC}}^2 / \gamma_{\text{LEP}}^2) \times (q_{\text{LEP}}^2 / q_{\text{LHC}}^2) \times (R_{\text{LEP}}^2 / R_{\text{LHC}}^2) \\
&\approx (1 \text{ TeV} / 0.2 \text{ TeV}) \times (m_p / m_e) \times (1) \times (1) \times (1) \\
&\approx 10^4,
\end{aligned} \tag{1.3}$$

which shows that the strength of the LHC bending magnets must be on the order of  $100\times$  the strength of those used at LEP. The magnetic fields experienced by the electron and positron beams at LEP were 0.22 Tesla. By Eqn. 1.3, the LHC bending magnets should achieve magnetic field strengths on the order of 10 Tesla in order to achieve the desired collision energies. The maximum achievable magnetic field of conventional ferrormagnets is about 2 Tesla. To meet the  $\sqrt{s} \approx 10$  TeV design goal, the magnet system used by the LHC to confine the protons to their circular orbits must then be composed of *superconducting* electromagnets. The entire magnet system of LEP was therefore removed and replaced with superconducting niobium-titanium (Nb-Ti) alloy based electromagnets which are superconducting at temperatures below 10 K. To reach temperatures below this 10 K threshold, the LHC magnets are housed in cryostats that allow for the Nb-Ti elements to be fully submerged in a bath of superfluid Helium at a temperature of 1.9 K [10]. In total, the LHC contains more than 120 tonnes of superfluid Helium. It goes without saying that there is a significant amount of resources and person power at CERN devoted to the refrigeration and cryogenics systems that are required for the LHC to run.

Additionally, the fact that LEP was a *particle-antiparticle* collider meant that the counter-rotating beams could be made to occupy a single ring: the same magnetic field could produce counter-rotating beams of electrons and positrons within the same beam pipe.<sup>6</sup> As a result, the LEP beam tunnel was constructed with only a single ring in mind and is relatively narrow: the LEP tunnel, and therefore LHC tunnel, is only  $\approx 3.7$  m wide on average. As the LHC is a *particle-particle* collider, it necessarily requires *two* magnetic fields of opposing polarity to circulate one of its beams in the clockwise direction and the other in the counter-clockwise direction. Given the limited space in the tunnel, however, it is not possible to house two separate rings of superconducting bending magnets with all of the services that they require *in addition* to the requisite minimal space needed for personnel and maintenance access. This forced the need of the so-called ‘2-in-1’ design of the main bending magnets of the LHC, wherein the two beam pipes are housed in the same cryostat in which the counter-rotating beams are held in their respective orbits by coupled magnetic fields. An illustration of this now-iconic design of the LHC bending (dipole) magnets and surrounding cryostat and containment structure is illustrated in Figure 1.3. Each of the 15 meter long superconducting dipole electromagnets of the LHC responsible for constraining the protons to their circular orbits

---

<sup>6</sup>The electrons and positrons at LEP were vertically separated within the beam pipe by electrostatic separators placed throughout the LEP ring. Turning off these separators is, to first approximation, how the LEP operators would get the electrically-attracting electrons and positrons to collide.

has currents of 11850 Amperes flowing through it and achieves magnetic field strengths of 8.33 Tesla.

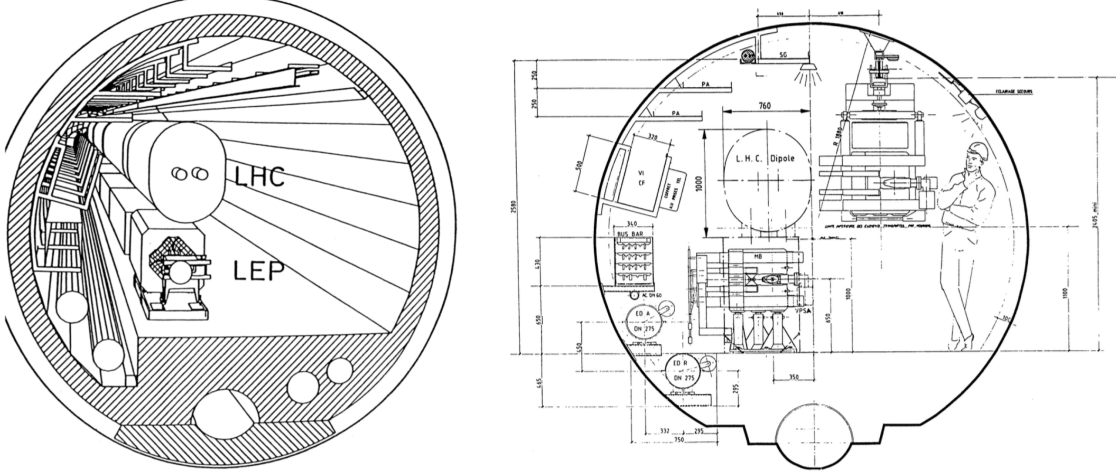


Figure 1.2: *Left:* Illustration comparing the size of a ‘2-in-1’ LHC dipole configuration to the LEP dipole and how they fit inside of the LEP/LHC tunnel. Note that prior to LHC operation, the LEP magnets will have been removed: the two are shown side-by-side for comparison purposes only. *Right:* Cross-sectional view of the LEP/LHC tunnel with a comparison of the LHC ‘2-in-1’ dipole on top of the LEP dipole. An illustration of an average size person is shown for scale. Also shown is the service crane in use, to give an idea of the size required for potential maintenance access. Clearly, two single-bore, superconducting rings each similar in size to the LEP dipole would not fit comfortably in the tunnel. The LHC ‘2-in-1’ design fits in nearly the same area as the LEP dipoles while additionally being able to contain both particle beams. Figures are taken from Ref. [11].

### Connecting the Dots

The LHC is essentially a chain of superconducting magnets of the type described in the previous paragraphs, where the bending (dipole) magnets critical to the LHC design were introduced. The chain is laid in a double-octagonal structure, illustrated in Figure 1.4. There are eight octants, at the center of which the LHC ring is straight and does not curve. The LHC curvature occurs at the boundaries of each of the octants and is primarily made up of bending (dipole) magnets. The straight sections are where the interaction regions are located and are referred to as ‘Points’, numbered 1 to 8. Points 1, 2, 5, and 8 are where the four large LHC experiments are located. Points 1 and 5 are home to the services and underground areas of the general purpose experiments, ATLAS and CMS, respectively. The underground experimental caverns associated with Point 1 and 5 were not present for LEP and had to be constructed after LEP was retired in 2000. Figure 1.5 provides an illustration of how the surface and underground areas are situated at Point 1. Points 2 and 8 host the services and underground areas of the ALICE and LHCb experiments, respectively. At these Points, Points 1, 2, 5, and 8, the counter-rotating beams are made to collide. The remaining Points, Points 3, 4, 6, and 7, are host to various beam ‘services’ necessary for the operation of the LHC. Point 3 and 7 host the beam betatron and momentum cleaning (‘beam collimation’) systems,

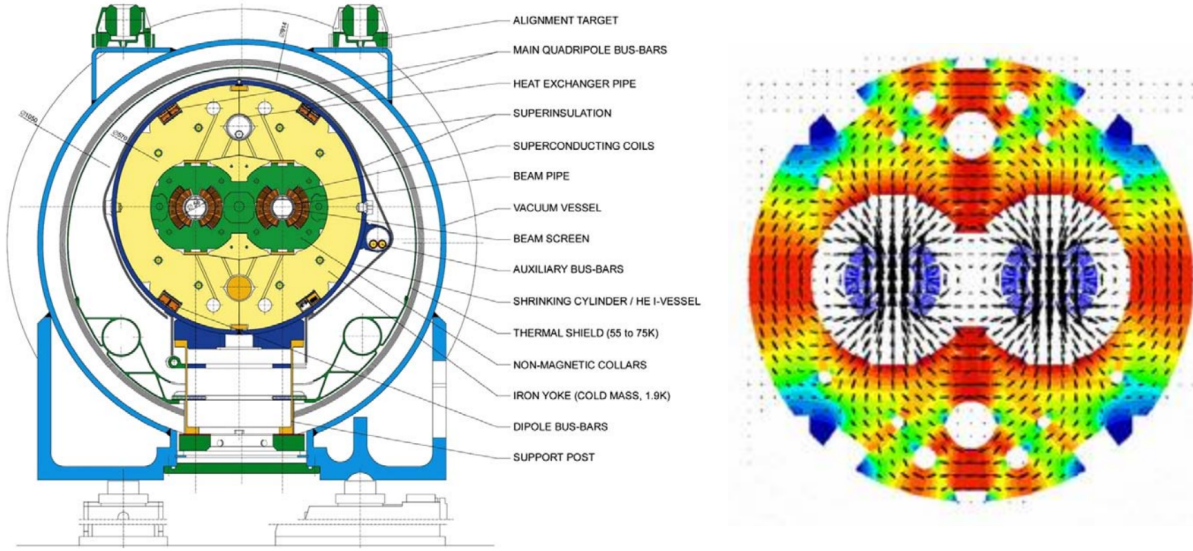


Figure 1.3: *Left:* Cross-sectional view of an LHC dipole bending magnet, with relevant parts indicated. The protons orbit inside of the beam pipes, each of which has a diameter of roughly 3 cm. It is interesting to note that the non-magnetic steel collars (in green) are of critical import to the success of the magnet systems. They are required to prevent the dipole structure from being deformed or torn apart due to the intense magnetic forces tending to push the two beam-pipes apart as a result of their counter-rotating electromagnetic currents. These forces amount to about 400 tonnes per meter of dipole when in full operation — almost equivalent in magnitude to the weight of a Boeing 747. *Right:* Magnetic field lines of the coupled dipole fields that bend the counter-rotating proton beams and keep them in their circular orbits around the LHC ring.

respectively. Point 4 hosts the superconducting radio-frequency (RF) systems which accelerate the beams to their nominal collision energies. Point 6 is the location of the beam-abort system — the so-called ‘beam dump’ — where the LHC beams may be removed very quickly from the LHC ring by using *kicker* magnets [12] that divert the beams out of the LHC ring in a safe manner. The beams may be dumped if the LHC wishes to refill with protons (or heavy-ions) and needs to remove any remnants of the previous fill, in case of beam instabilities observed in the LHC ring, or if one of the experiments signals the need for a beam dump (in case of beam stability or detector issues observed at the associated IP).

### 1.1.2 Injection Chain and Bunch Structure

We now have an idea of how the proton beams relevant to the work in this thesis are made to circulate in the LHC ring. In this section we will briefly describe the initial source of the protons and how they are introduced into the LHC ring. The LHC relies on a series of pre-acceleration steps that bring the initial low-energy protons to energies sufficient enough to begin their journey through the LHC. The sum-total of these steps is referred to as the LHC *injection chain* [14]. The components of the LHC injection chain form the heart of the CERN accelerator complex illustrated

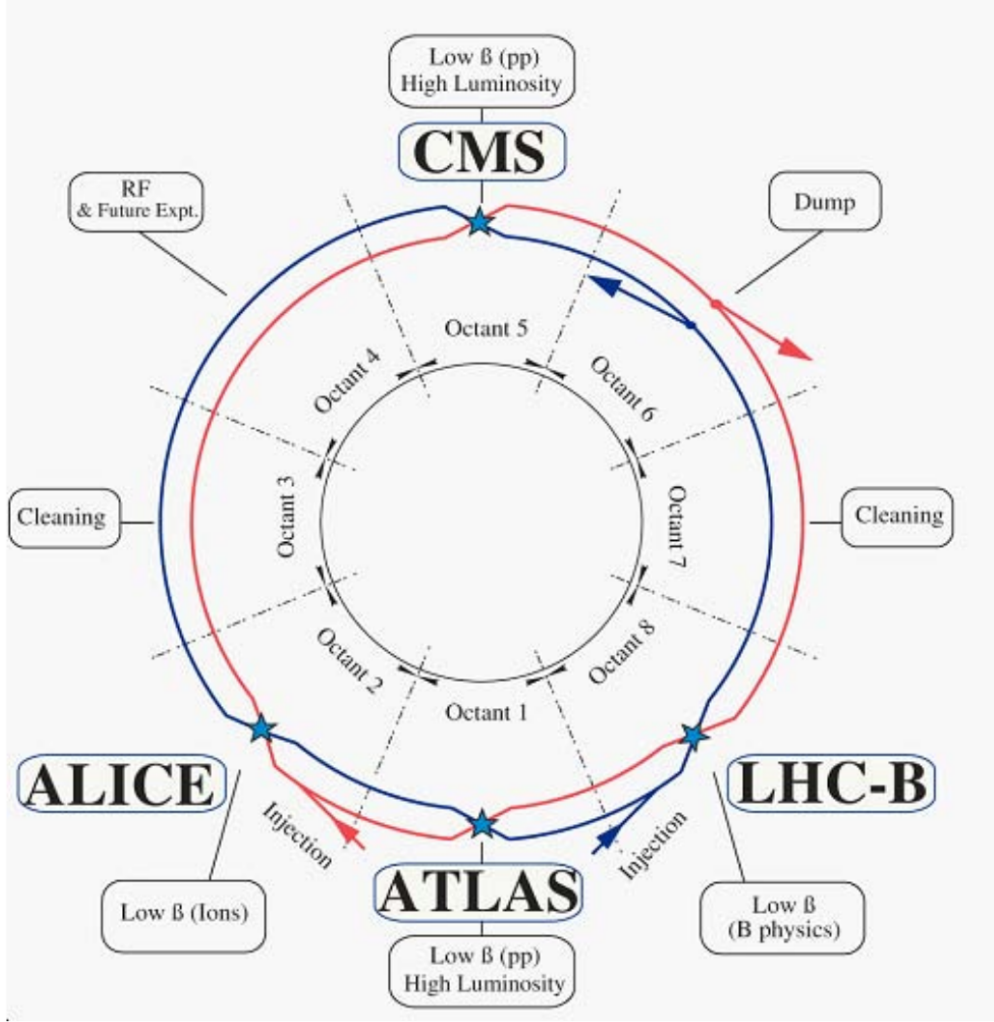


Figure 1.4: Layout of the LHC and its two counter-rotating beams. Beam 1 is in blue and rotates counter-clockwise. Beam 2 is in red and rotates clock-wise. At the center of each octant is a straight section which houses the experimental caverns or LHC beam facilities. At the boundaries of each octant are located the curved sections. Figure taken from Figure 2.1 of Ref. [6]. **Somewhere  $\beta$  should be described – betatron function**

in Figure 1.1. For  $pp$  collisions in the LHC, the protons are initially sourced from Hydrogen atoms that are released at the start of Linac 2. The Hydrogen atoms are immediately stripped of their electrons after passing through the *duoplasmatron* ion source [15]. The protons are then passed through Linac 2, a linear accelerator, which accelerates the protons to 50 MeV. They then enter the Proton Synchotron Booster (PSB), a circular storage ring composed of four stacked rings, which accelerates the protons to 1.4 GeV. The PSB injects the protons into the Proton Synchotron (PS) which accelerates them to 25 GeV. The Super Proton Synchotron (SPS) receives the protons from the PS and accelerates them to 450 GeV. At this point the protons have sufficient energy to be injected into the LHC. There are two injection points into the LHC since, up until this

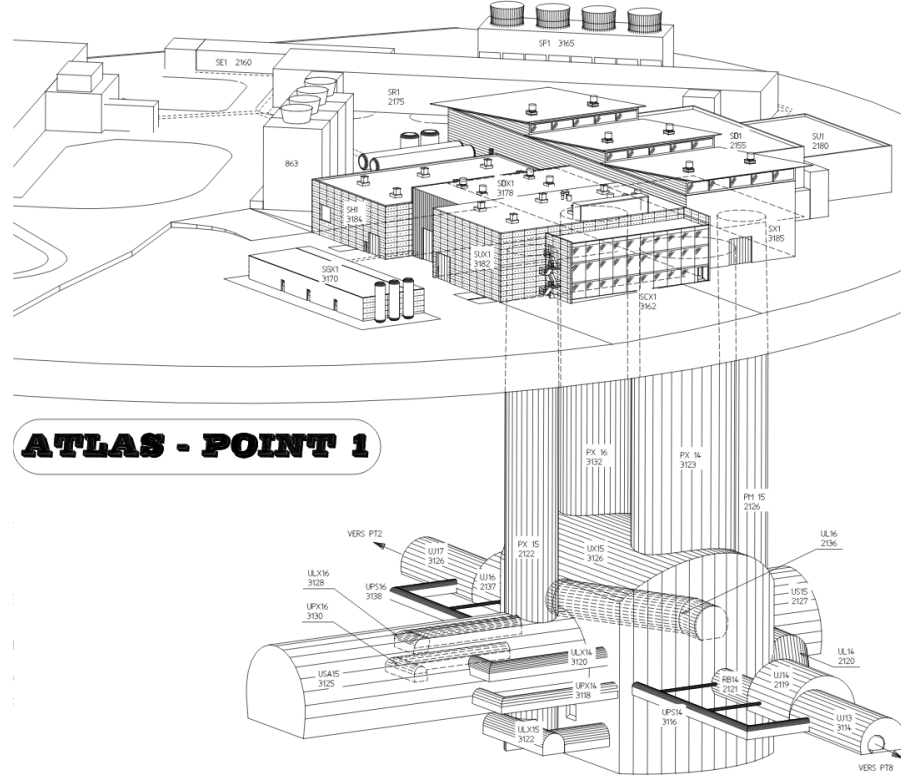


Figure 1.5: Diagram showing the surface buildings and services and underground areas of Point 1, where the ATLAS experiment is located. The LHC ring can be seen at the bottom, with its directions indicated by the ‘VERS PT8 (2)’ arrows pointing towards Point 8 (2). The experimental cavern in which the ATLAS detector sits is UX15. The control room for the ATLAS experiment, whereat operators can monitor and control the state of the ATLAS detector, is located 100 m above UX15 in the building SCX1. Figure taken from Figure 10.1 of Ref. [13].

stage, the protons are circulating in the same direction: one injection point sends protons into the counter-clockwise beamline of the LHC, and the other into the clockwise beamline. Until all of the protons from a single *fill* make their way into the LHC, they will circulate at the injection energy of 450 GeV. After the filling completes<sup>7</sup>, the superconducting RF cavities located at Point 4 will begin to accelerate the protons to their final collision energies.<sup>8</sup> The acceleration is achieved by increasing the frequency of the RF oscillations; however, given that a 450 GeV proton is already ultra-relativistic, the adjustment of the frequency needed to get to the collision energies is not large but still has consequences for the design of the detector and measurement apparatus along the LHC ring [16].

The proton beams circulating the LHC are not a continuous stream of protons; rather, they are grouped into what are referred to as *bunches*. The protons arrive at the LHC in these bunches which are initially prepared in the smaller machines that make up the LHC injection chain and

<sup>7</sup>A standard LHC fill takes on the order of 4 minutes per ring.

<sup>8</sup>If all goes smoothly, this acceleration stage takes roughly 20 minutes.

then are kept in their final *bunch structure* by the RF cavities. The accelerating RF cavities provide an accelerating electromagnetic field that oscillates longitudinally. The bunches, each composed of roughly  $10^{11}$  protons, are then made to oscillate longitudinally in so-called *synchotron oscillations* around the central node of the RF oscillation as they circulate through the LHC ring. The proton bunches are then effectively ‘shaped’ by the oscillating RF field: protons in a bunch lagging behind or that are ahead of those particles at the center of the bunches will be accelerated or decelerated accordingly so as to be pushed back into the center of the bunch. The LHC RF cavities have an oscillation frequency of 400 MHz which defines the boundaries in which proton bunches can lie. These boundaries are called *RF buckets* and, along with the circumference of the LHC, dictate the number of proton bunches that can potentially fit in the LHC. The relationship between the RF oscillations and the RF bucket and bunch structure is illustrated in Figure 1.6. In total, approximately 35640 RF buckets exist when the LHC is in operation. Not all buckets contain proton bunches, however. In fact, at the time of the writing of the present thesis, RF buckets filled with proton bunches have a minimal separation of 10 RF buckets, meaning that following an RF bucket containing a proton bunch there is at least 9 unfilled RF buckets. This corresponds to a minimal time between proton bunches — the *bunch spacing* — of 25 nanoseconds. At the time of the present thesis, the operating conditions of the LHC maximally allow for 2808 25 ns-spaced bunches.<sup>9</sup> The bunch-spacing and overall bunch structure of an LHC fill is not only decided by the operators of the LHC but also by what the detectors at Points 1,2,5, and 8 can tolerate. This is because shorter bunch spacing means higher intensity and multiplicity of collisions occurring at each of these IP. A 25 nanosecond bunch spacing corresponds to a maximal  $pp$  collision rate of 40 MHz. The detectors at each of the IP have been designed with this collision rate in mind and anything higher may push them beyond their design limits.

### 1.1.3 The Concept of Luminosity

In designing a particle collider, the collision energy is not the only important parameter. Equally important is the value of the instantaneous *luminosity* that can be achieved by the collider. An expression for the instantaneous luminosity,  $\mathcal{L}$ , is given by,

$$\mathcal{L} = \frac{N^2 n_b f}{4\pi\sigma_x\sigma_y} \cdot S, \quad (1.4)$$

where  $N$  is the number of particles per bunch,  $n_b$  is the number of colliding bunches,  $f$  is the bunch revolution frequency,  $\sigma_{x,y}$  are the transverse beam widths in the Gaussian approximation, and  $S$  is a reduction factor that accounts for geometric factors such as the non-zero crossing-angle

---

<sup>9</sup> The number of allowed bunches is significantly lower than the 35640 RF buckets with 25 ns bunch-spacing potentially allow for. This is due, in part, to the non-trivial bunch-structure typically employed but also in large part to the fact that there is a  $\approx 30\ \mu s$  *abort gap* in the LHC ring where no filled RF buckets exist. The abort gap is a number of continuous unfilled RF buckets that allows the ramp up of the kicker magnets used for the beam dump to occur in the absence of filled buckets. In this way, the kicker magnet ramp up does not disturb the structure of the circulating proton beams. Only after this ramp up is finished should the kicker magnets disturb the beams.

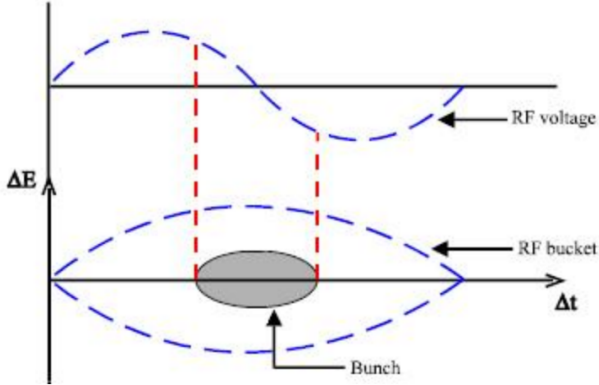


Figure 1.6: Illustration of the particle bunch structure in a particle collider such as the LHC. The particles are accelerated by radio-frequency (RF) oscillations whose amplitude is illustrated in the upper plot. The RF bucket's boundary, illustrated in the lower plot, is defined by a full period of the RF oscillation and the particle bunch formation, depicted in grey, occurs at the central node of the oscillation. The area occupied by the particle bunch is related to the beam's longitudinal *emittance*.

of the colliding beams [14, 17]. The instantaneous luminosity,  $\mathcal{L}$ , can be seen by Eqn. 1.4 to have units of  $\text{cm}^{-2}\text{s}^{-1}$  and can be conceptually thought of as the outgoing flux of particles per unit area and time after a bunch crossing in which successful  $pp$  collisions occur. The LHC is designed to deliver collisions to the high luminosity IP (Fig. 1.4) at  $\mathcal{L} = 10^{34} \text{ cm}^{-2}\text{s}^{-1}$ . Accurate knowledge of  $\mathcal{L}$  is of the utmost importance for collider design and operation. Not only does it parametrise the potential collision rate once the collider beam and bunch structure are decided, but it allows for the accurate prediction of the number of collision events,  $N_{\text{proc}}$ , associated with a particular physics process with cross-section  $\sigma_{\text{proc}}$ ,

$$N_{\text{proc}} = \sigma_{\text{proc}} \int \mathcal{L} dt \equiv \sigma_{\text{proc}} \cdot L, \quad (1.5)$$

where  $L$  is referred to as the *integrated luminosity* and has units of  $\text{cm}^{-2}$ . A common unit for integrated luminosity is the *barn*, with symbol ‘b’: one barn is defined as  $10^{-24} \text{ cm}^{-2}$ . The datasets collected so far by the LHC experiments are such that the *femtobarn* (fb),  $10^{-39} \text{ cm}^{-2}$ , is relevant.

#### 1.1.4 Operation of the Large Hadron Collider

The LHC has been in stable operation since 2009. It operates in so-called *runs*: multi-year periods of roughly continuous data-taking. As CERN shuts down during the winter months, each run is segmented each year with a several month long shutdown in the winter with a ramp-up period in the spring. During these shorter shutdowns, maintenance and upgrades may take place. In between a given run there is a multi-year break, a *long shutdown*, in which large(er)-scale maintenance and upgrades of both the LHC and the experiments can take place. At the time of writing, there has so

far been two runs of the LHC, Run-I and Run-II. Run-I took place during the years 2009–2012 and Run-II during 2015–2018. The integrated luminosities for each of the data taking years between Run-I and Run-II is shown in Fig. 1.7. The data relevant to the work presented in this thesis were collected in both Run-I and Run-II of the LHC, specifically that data collected in the years 2012–2018. The luminosities, instantaneous and integrated, as well as the center-of-mass collision energies,  $\sqrt{s}$ , for these data-taking periods are shown in Table 1.1. Also shown in Table 1.1 are the average values of the mean number of interactions per bunch crossing,  $\langle\mu\rangle$ , observed during each data-taking year. The quantity  $\langle\mu\rangle$  is related to the amount of *pileup* observed during data-taking. Pileup is caused by overlapping  $pp$  interactions within the same (*in-time* pileup) or neighboring (*out-of-time* pileup) bunch-crossing(s) at the interaction point. The pileup scales with the instantaneous luminosity. Distributions of  $\langle\mu\rangle$  are shown in Fig. 1.7 for the Run-II data-taking period.

	<b>Run-I</b>	<b>Run-II</b>			
Year	2012	2015	2016	2017	2018
Collision energy, $\sqrt{s}$ [TeV]	8			13	
Peak Luminosity, $\mathcal{L}$ [ $\text{cm}^{-2}\text{s}^{-1}$ ] ( $\times 10^{34}$ )	0.77	0.5	1.4	2.1	2.1
Integrated Luminosity, $L$ [ $\text{fb}^{-1}$ ]	20.2	3.2	33.0	44.3	59.9
Mean number of interactions per bunch crossing, $\langle\mu\rangle$	20.7	13.4	25.1	37.8	36.1

Table 1.1: Summary parameters for the data-taking periods relevant to the work presented in this thesis. The integrated luminosity is that relevant to performing physics analysis and potentially differs with respect to the total integrated luminosity delivered to ATLAS by the LHC (Fig. 1.7) due to the application of strict quality criteria on the data prior to its use in physics analyses.

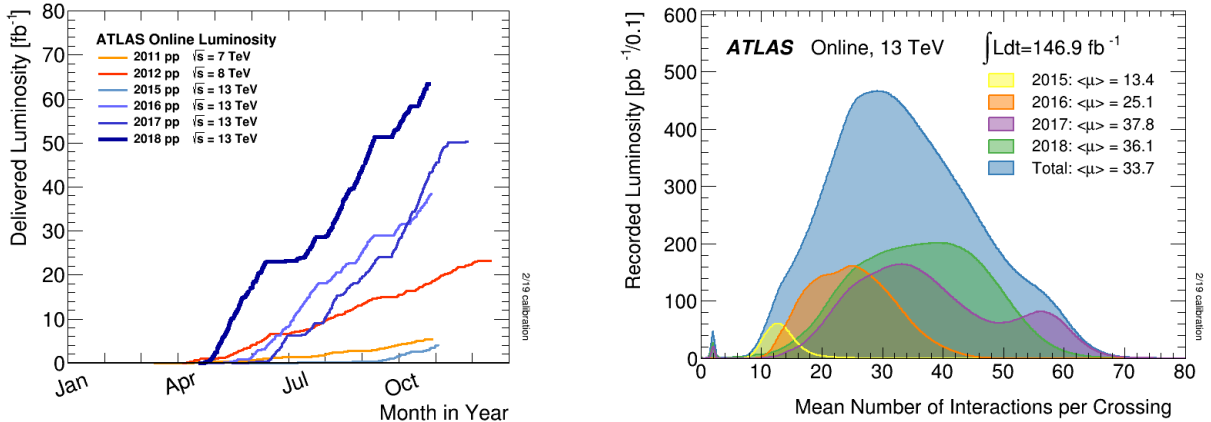


Figure 1.7: *Left:* The ATLAS integrated luminosity during the data-taking years 2011–2018. *Right:* The observed average number of  $pp$  interactions per bunch-crossing,  $\langle\mu\rangle$ , observed by ATLAS during the Run-II data-taking years, 2015–2018.

## 1.2 The ATLAS Detector

In this section we will extend our focus to the ATLAS detector, the general purpose particle detector located at Point 1 of the LHC ring (see Figure 1.5). Roughly cylindrical in shape, coaxial with the beam-pipe, the ATLAS detector is 44 m long and 25 m tall. It is by far the largest such detector ever built and, generally, is the largest and most complex device ever constructed. Being general purpose in scope, the ATLAS detector is hermetic and has nearly  $4\pi$  radians of solid angle coverage around the  $pp$  collision point. Such detectors are commonly designed to have various subsystems — *subdetectors* — which are designed for the identification of specific types of particles and interactions. They tend to be layered about the interaction point and cylindrically symmetric since the  $pp$  interactions taking place within the detector have no preferred direction in the plane transverse to the direction in which the proton beams are travelling. A view of the ATLAS detector and its subdetectors is provided by Figure 1.9. In the following we will briefly describe each subsystem in turn, describing first the detectors located nearer to the  $pp$  collision and proceeding outwards.

### 1.2.1 The ATLAS Coordinate System

The ATLAS detector uses a right-handed coordinate system with the origin located at the geometric center of the detector. The  $x$ -axis points to the center of the LHC ring, the  $y$ -axis points upwards and away from the center of the Earth, and the  $z$ -axis is along the beam-pipe. The side associated with positive (negative)  $z$  is referred to as the ‘A’ (‘C’) side of the detector.<sup>10</sup> Due to its cylindrical symmetry, ATLAS also uses the cylindrical coordinates,  $(r, \phi, z)$ , with  $\phi$  the azimuthal angle about the  $z$ -axis and having  $\phi = 0$  along the positive  $x$ -axis. The spherical polar angle,  $\theta$ , is defined with respect to the  $z$ -axis, having  $\theta = 0$  parallel to the beam-pipe and  $\theta = \pi/2$  in the  $xy$ -plane transverse to the beam-pipe. The pseudorapidity,  $\eta$ , is commonly used when describing systems of particles or locations within the detector and is defined as  $\eta = -\ln [\tan(\theta/2)]$ . The relationship between pseudorapidity and polar angle is illustrated in Figure 1.8. Large (small) values of  $\eta$  correspond to the *forward* (*central*) region of the detector. The rapidity,  $y$ , is related to  $\eta$  and is defined as  $y = \frac{1}{2} \ln [(E + p_z)/(E - p_z)]$ . The pseudorapidity of a particle traversing the detector is equal to its rapidity if the particle is massless or ultra-relativistic; otherwise, they are different. The comparison between a particle’s pseudorapidity and rapidity is illustrated in Figure 1.8. The coordinates used to describe systems of particles are typically described by their four-momenta:  $(p_x, p_y, p_z)$  or, equivalently,  $(p_T, \eta, \phi)$ . A distance metric commonly used to describe the distance between two systems of particles in the detector is  $\Delta R = \sqrt{(\Delta\eta)^2 + (\Delta\phi)^2}$ . The  $\Delta R$  quantity using  $y$  instead of  $\eta$  is also sometimes used and will be indicated by  $\Delta R_y$ .

---

<sup>10</sup>‘A’ for ‘airport’, since this is the side pointing towards Geneva International Airport, and ‘C’ for either ‘Crozet’ or ‘Charly’s’, depending on who you ask, since this is the side pointing towards the town of Crozet and/or Charly’s Pub in the town of Saint-Genis-Pouilly.

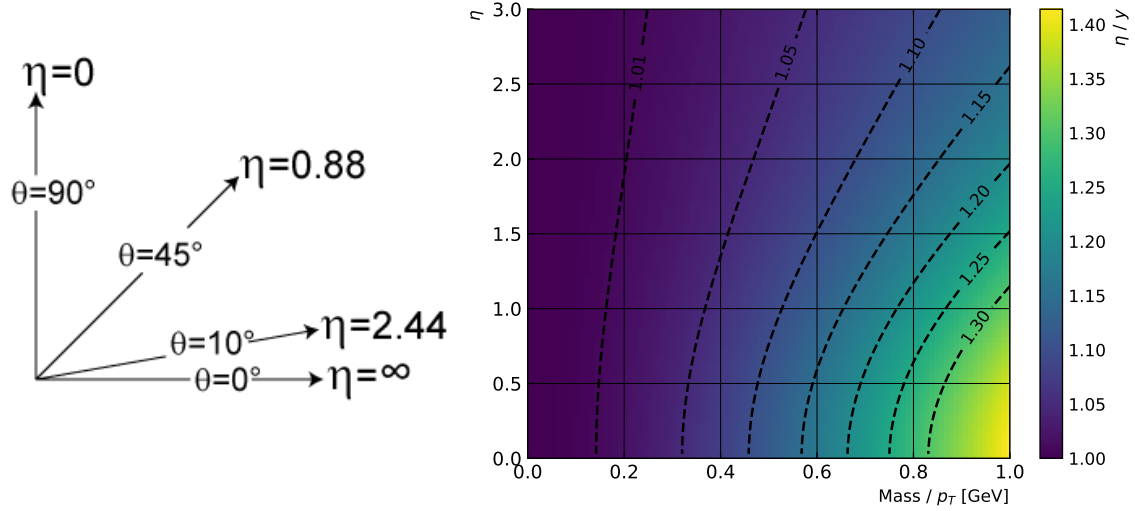


Figure 1.8: *Left*: Illustration of the relationship between the pseudorapidity,  $\eta$ , and polar angle,  $\theta$ , defined as the angle with respect to the beam-axis ( $z$ -axis). *Right*: Distribution of the ratio of a particle's pseudorapidity to its rapidity,  $\eta/y$ , as a function of its pseudorapidity ( $y$ -axis) and the ratio of its mass to its transverse momentum,  $p_T$  ( $x$ -axis).

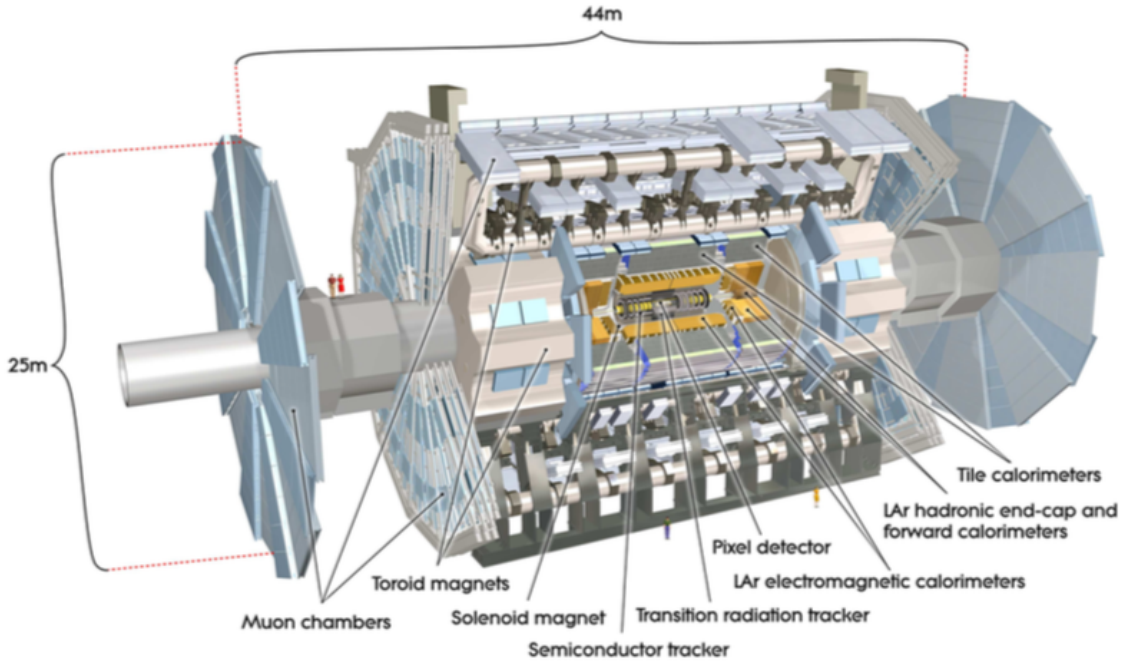


Figure 1.9: Cut-away view of the ATLAS detector with sub-systems indicated. Shown for comparison are figures of average-height humans standing at the feet of the detector and standing on the forward shielding between the big wheels of the forward muon system.

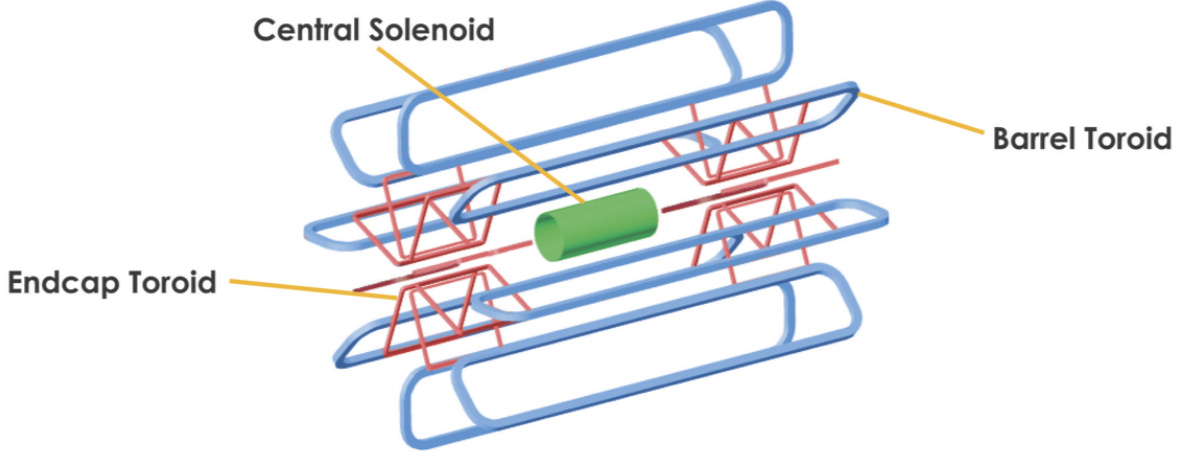


Figure 1.10: A view of the ATLAS magnet system. Shown are the 2 T solenoid magnet in green, the barrel toroid system in blue, and endcap toroid magnets in red.

### 1.2.2 The Inner Detector

The innermost subdetector of ATLAS is the Inner Detector (ID) [18]. The ID covers the region  $|\eta| < 2.5$  and is composed, in order of increasing radial distance from the beam-pipe, of the pixel detector, semiconductor tracker (SCT), and the transition radiation tracker (TRT). These detectors enable the reconstruction of the tracks associated with the  $\mathcal{O}(1000)$  charged particles emerging from each  $pp$  bunch collision occurring every 25 ns. An illustration of the ID and its subdetectors is shown in Figure 1.11. Additional, more detailed views of the barrel and endcap sections of the ID are shown in Figure 1.12. The ID is situated inside of the central solenoid, indicated in Figure 1.10, which provides an axial 2 T magnetic field and extends over a length of 5.3 m with a diameter of 2.5 m. The bending of charged particles in the  $xy$ -plane due to the presence of the solenoidal field allows for their momenta to be measured using the curvature of their reconstructed tracks.

#### The Pixel Detector and IBL

The pixel detector is the innermost subdetector of the ID, situated very near to and surrounding the beam-pipe. It is composed of three separate sections: a barrel section and two end-cap sections. The barrel section of the pixel detector has a cylindrical geometry and the end-cap sections are disks centered on the beam-pipe. The barrel section has four layers, each with increasing radius, and there are three disks in each of the end-caps. This ID geometry, shown in Figure 1.12, covers the region  $|\eta| < 2.5$ .

The pixel detector, being so near the  $pp$  collisions, is subject to the highest particle fluxes of any other subsystem. As a result, it is built to have very fine granularity: its sensing elements consist of  $250\ \mu\text{m}$  thick detectors housing pixels of reverse-biased n-type silicon semiconductor material, each having a nominal size of  $50 \times 400\ \mu\text{m}^2$ . In total, there are roughly 80 million channels read out from the pixel detector alone. This allows for the pixel detector's fine spatial hit resolution of

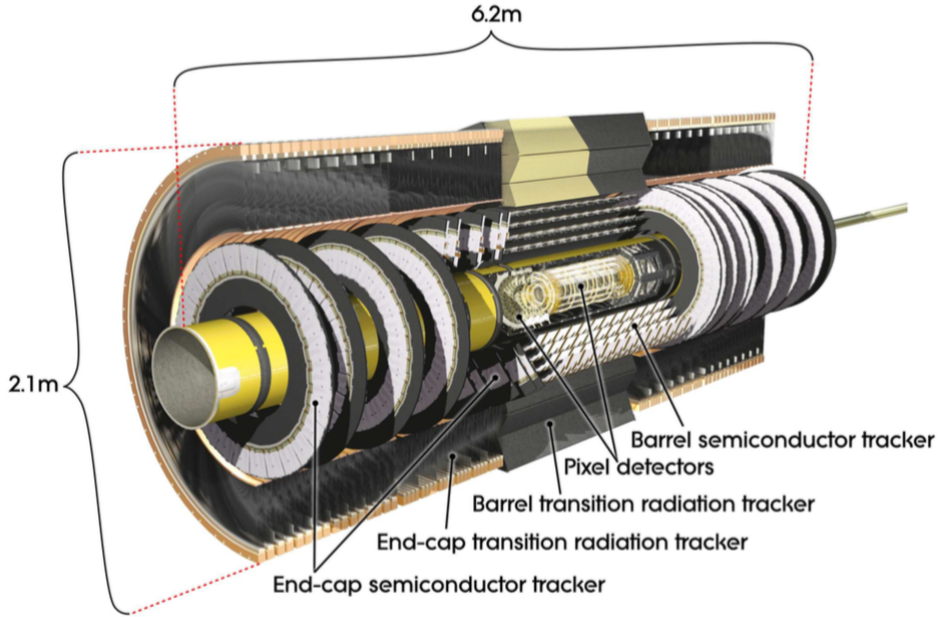


Figure 1.11: Cross-sectional view of the ATLAS inner detector. Shown are the barrel and end-cap portions of the pixel, SCT, and TRT detectors.

$10 \mu\text{m}$  in  $(r - \phi)$  and  $115 \mu\text{m}$  along  $z$ .

The innermost layer of the pixel detector's barrel section is referred to as the *Insertable B-Layer* (IBL), and was installed at the beginning of the Run-II data-taking period [19]. It corresponds, essentially, to the instrumentation of the ATLAS beam-pipe, as seen in Figure 1.14, and is located at a radial distance of 3.3 cm. It alone accounts for 8 million readout channels of the pixel detector — resulting in an ultra precise spatial hit resolution of  $8 \mu\text{m}$  in  $(r - \phi)$  and  $40 \mu\text{m}$  along  $z$ . Beyond improving the overall measurements and reconstruction of charged particle tracks, the IBL was installed in order to improve the performance of secondary vertex reconstruction — an essential ingredient to the algorithms associated with the reconstruction and identification of jets originating from the decays of  $b$ -hadrons whose decays occur at radial distances frequently beyond that of the IBL.

### The Semiconductor Tracker

The semiconductor tracker (SCT), like the pixel detector, uses silicon semiconductor-based sensing elements. It surrounds the pixel detector, as illustrated in Figure 1.12, and has similar barrel and end-cap geometries. The barrel section of the SCT is composed of 4 cylindrical layers and the end-caps consist of 9 disks. The silicon sensing elements are in a strip-like geometry with  $80 \mu\text{m}$  strip pitch. The strips in the barrel section run parallel to the beam-pipe and those in the end-caps

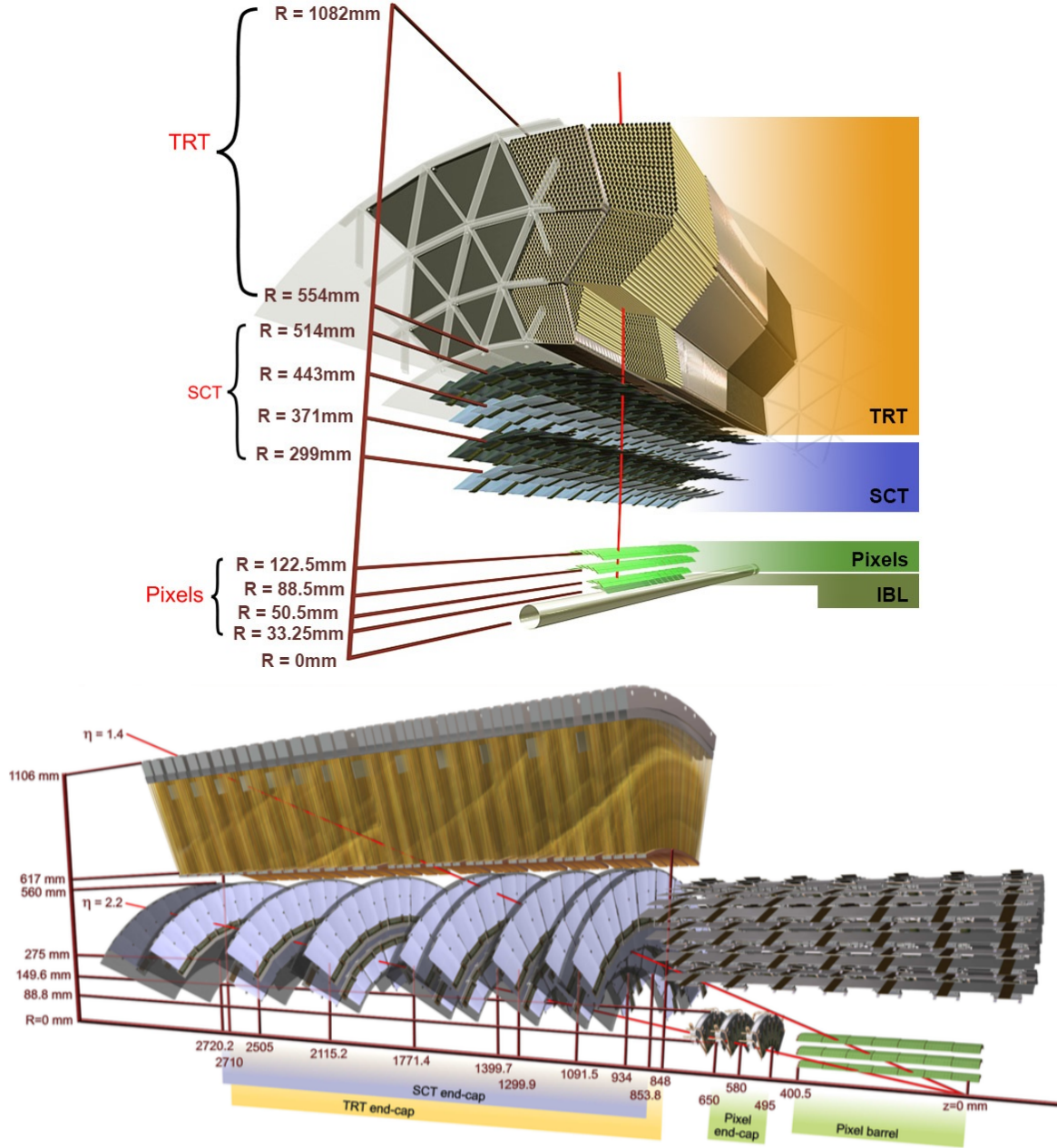


Figure 1.12: Cut-away views of the barrel (top) and end-cap (bottom) portions of the ATLAS inner detector, with each of the three subdetectors indicated along with their envelopes in  $r$  and in  $z$ .

are perpendicular, extending along the radial direction.<sup>11</sup> The spatial hit resolution of the SCT is

<sup>11</sup> The SCT layers in both the barrel and end-cap sections additionally contain small-angle (40 mrad) stereo strips to allow for measurement of both ( $r - \phi$ ) and  $z$  information.

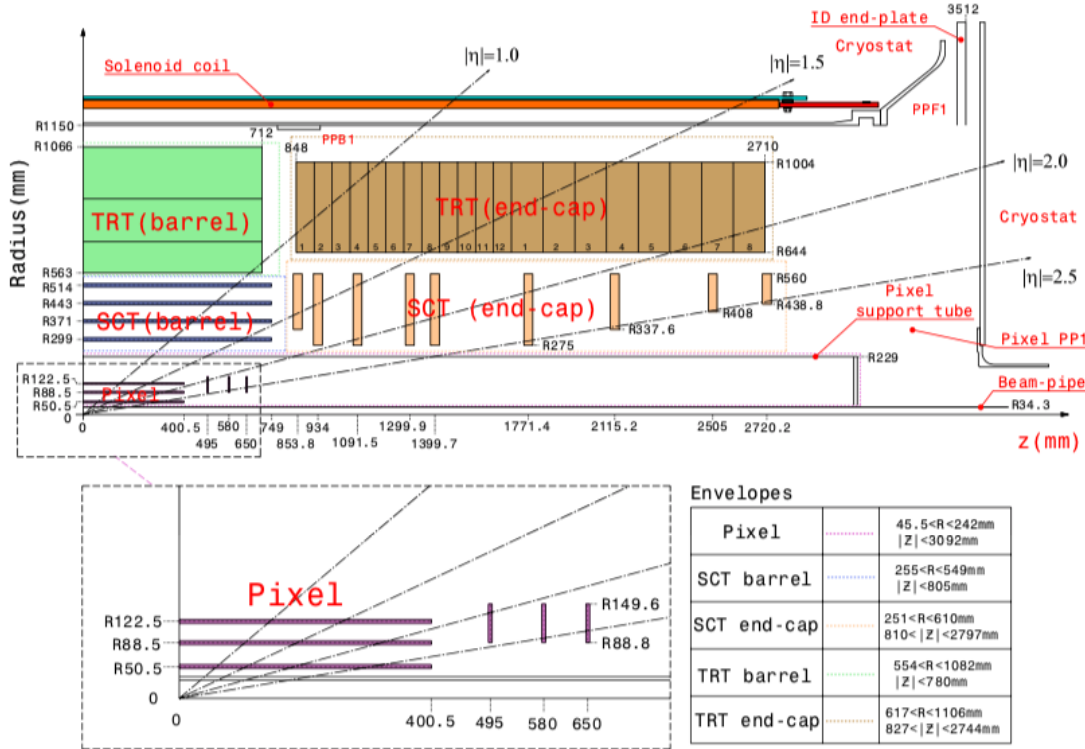


Figure 1.13: From Ref. [5].

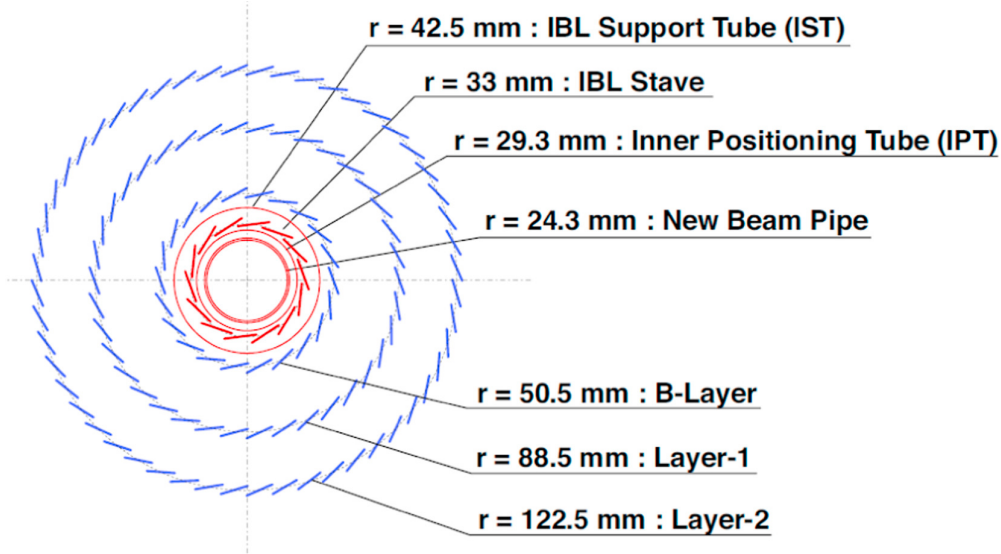


Figure 1.14: Transverse view of the barrel section of the pixel detector, showing the innermost layer, the Insertable B-Layer (IBL), and its support structure (red) as well as the three surrounding layers (blue). From Ref. [20].

$17\ \mu m$  in  $(r - \phi)$  and  $580\ \mu m$  along  $z$ .

### The Transition Radiation Tracker

The outermost layer of the ATLAS ID, surrounding the SCT, is the transition radiation tracker (TRT). The TRT is a tracking volume designed around the proportional drift tube concept and is composed of polyimide drift tubes (straws) that are 4 mm in diameter. The barrel section of the TRT contains up to 73 layers of 144 cm-long straws aligned parallel to the beam-pipe while the end-cap section has 160 straw planes composed of 37 cm long straws arranged radially into wheels (see Figure 1.12). Each straw of the TRT has a  $37\ \mu m$  gold-coated wire at its center which acts as anode and is grounded, while the inner walls of each straw are kept at a potential of approximately  $-1.5\ kV$ . A track hit in a given straw is the result of the  $70\% \text{ Xe} - 27\% \text{ CO}_2 - 3\% \text{ O}_2$  gas mixture contained in the straw volume being ionised and the resulting electrons (ions) drifting to the center wire (inner wall) of the straw. The induced current from the drifting charge is converted to an electrical signal and read out.

On average, a single charged-particle track leaves 36 hits in the TRT. The TRT only provides  $(r - \phi)$  information (no  $z$  information), for which it has a per-straw hit resolution of  $130\ \mu m$ . The relatively poor hit resolution, when compared to the silicon based tracking detectors, is compensated by the large number of hits per track which lead to very long measured track lengths as compared to the pixel and SCT detectors. Additionally, the straws are embedded in and individually separated by a polypropylene fiber which induces transition-radiation photons to be produced. The amount and pattern of transition radiation depends on the mass of the passing particle: the passage of an electron will produce significantly more transition radiation than heavier charged particles, such as the copiously-produced pion. Information provided by the TRT therefore provides additional discrimination power between electrons and pions and enhances the performance of ATLAS' electron identification algorithms that primarily depend on information coming from the calorimeter systems (Section 1.2.3).

### 1.2.3 Calorimeter Systems

The ATLAS calorimeter systems are situated outside of the ID and central solenoid and are tasked with the measurement and containment of showers from electrically charged and neutral particles. A view of the calorimeter systems is provided by Figure 1.15. Broadly speaking, there are two types of calorimeters based on their purpose: electromagnetic and hadronic calorimeters. The electromagnetic calorimeter system has  $\eta$  coverage that matches the inner-detector and is optimized for precision measurements of electrons and photons. The hadronic calorimeter system has readout cells that are generally of coarser granularity as compared to the electromagnetic calorimeter and is designed to meet the requirements for jet and missing transverse momentum measurements. Besides classification by physics purpose, the calorimeter system can also be broken into two classes based on detector technology: either based on gaps of cooled liquid-argon [21] or on scintillating tiles as the active media [22].

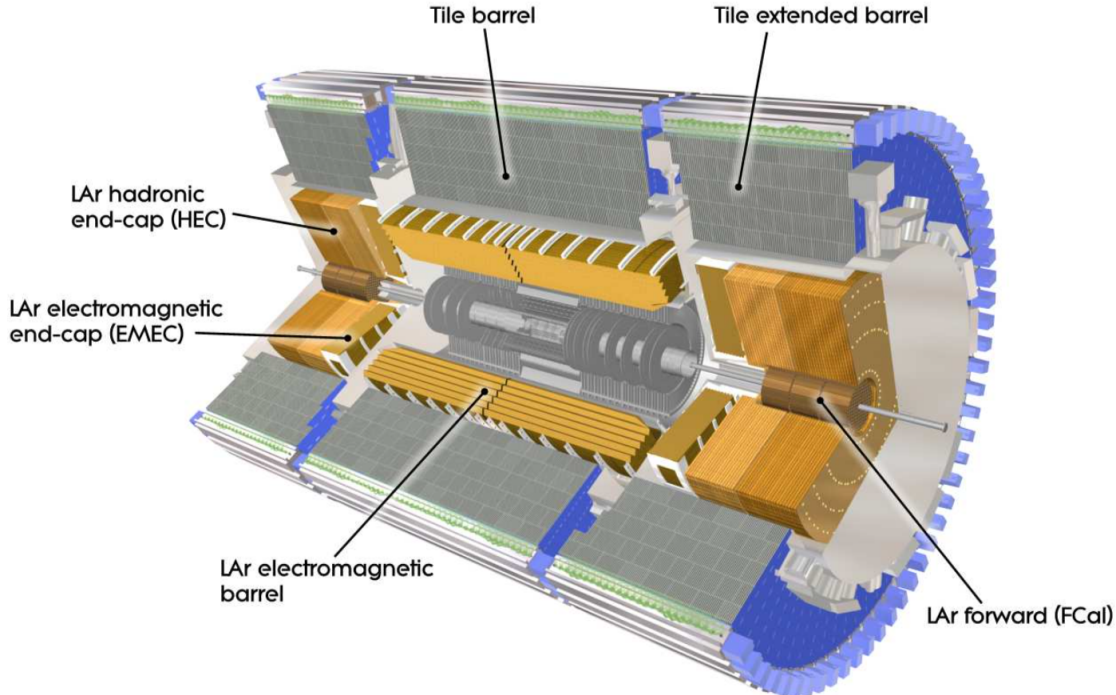


Figure 1.15: Cut-away view of the ATLAS calorimeter system, with liquid-argon and scintillating-tile subsystems indicated.

### Electromagnetic Calorimeter

The electromagnetic (EM) calorimeter is a high-granularity lead/liquid-argon (LAr) sampling calorimeter situated outside of the ID and sharing the same cryostat as the the central solenoid. It consists of barrel and end-cap sections that cover the entire range within  $|\eta| < 3.2$  and is illustrated in Figure 1.15. The structures of the electromagnetic barrel and end-cap calorimeters are shown in Figure 1.16. The EM calorimeter is designed in an accordian type structure to provide full coverage in  $\phi$ . The cooled LAr fills the gaps between layers of the accordian structure. Passing particles from the interaction point undergo scattering and bremsstrahlung processes as they pass through the lead absorbers. The resulting electrons and photons ionise the LAr, producing drift electrons and ions whose signals are read out by the interleaved readout electrodes. The 2.1 mm drift gap has an operating voltage of  $\approx 2\text{ kV}$ . The electromagnetic calorimeter is  $> 22$  radiation lengths ( $X_0$ ), ensuring that the majority of electrons and photons are completely contained within the EM calorimeter. The majority of the EM energy, amounting to approximately  $16 X_0$ , is contained within the second sampling layer (see Figure 1.16). The fine granularity of the readout, indicated in Figure 1.16, was designed with the ability to distinguish individual photons arising from  $\pi^0 \rightarrow \gamma\gamma$  decays. The ability to distinguish photons pairs so precisely is also important for the main Higgs boson decay channel used for its discovery,  $h \rightarrow \gamma\gamma$ .

In the region  $|\eta| < 1.8$ , a so-called *presampler* detector is used to correct for the energy lost by

electrons and photons due to material interactions occurring upstream of the EM calorimeter. It is a single LAr layer, with width 1.1 cm (0.5 cm) in the barrel (end-cap).

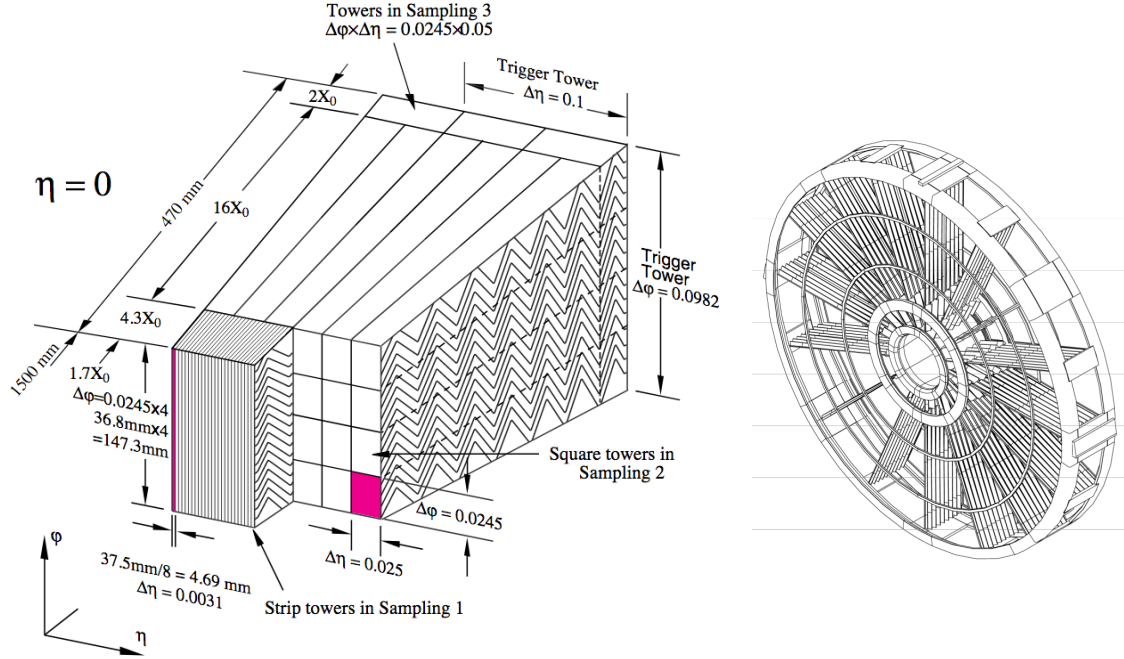


Figure 1.16: *Left:* Cut-away view of the barrel electromagnetic calorimeter and its accordian structure. Indicated are the geometry and absorption properties of the three sampling layers. Also indicated is the granularity of the electrode readout in  $\Delta\phi \times \Delta\eta$  in each layer. *Right:* Diagram of the electromagnetic end-cap calorimeter accordian wheel structure (only a sub-set of the accordian structure is shown).

## Hadronic Calorimeter

The barrel section of the hadronic calorimeter is composed of a lead/scintillating-tile type detector whereas the end-cap hadronic calorimeter is based on copper/LAr-based technology.

The lead/scintillating-tile calorimeter (the ‘tile calorimeter’) is located just beyond the EM calorimeter. It is composed of a barrel section, covering  $|\eta| < 1.0$ , and two extended barrels that cover  $0.8 < |\eta| < 1.7$  (see Figure 1.15). It is a sampling calorimeter using steel as the passive absorber and scintillating plastic tiles as the active media. The tile calorimeter is composed of modules in which the scintillating tiles are situated in  $(r - \phi)$  within the steel absorbers, as shown in Figure 1.17. The detector is segmented radially into three layers and the readout of the scintillation light, using wavelength-shifting fibers that are fed into photomultiplier tubes (PMT) situated along the outer radii, is organized in a projective geometry, also illustrated in Figure 1.17. In the barrel (extended barrel) section, most of the hadronic energy is captured by the first (last) two layers which account for  $\approx 5.5$  (6) hadronic interaction lengths ( $\lambda$ ) of the  $\approx 7$  in total.

The hadronic end-cap (HEC) calorimeter consists of two wheels per end-cap, situated behind the electromagnetic end-cap calorimeter, and provides calorimetric coverage in the range  $1.5 < |\eta| < 3.2$ . A view of the HEC can be seen in Figures 1.15 and 1.18. The HEC calorimeter is built from layers of copper plates interleaved with 8.5 mm LAr gaps which provide the active medium for this sampling calorimeter. The readout structure is obtained by dividing the gaps into separate drift zones for which there are dedicated readout electrodes. This readout structure is arranged in a projective geometry.

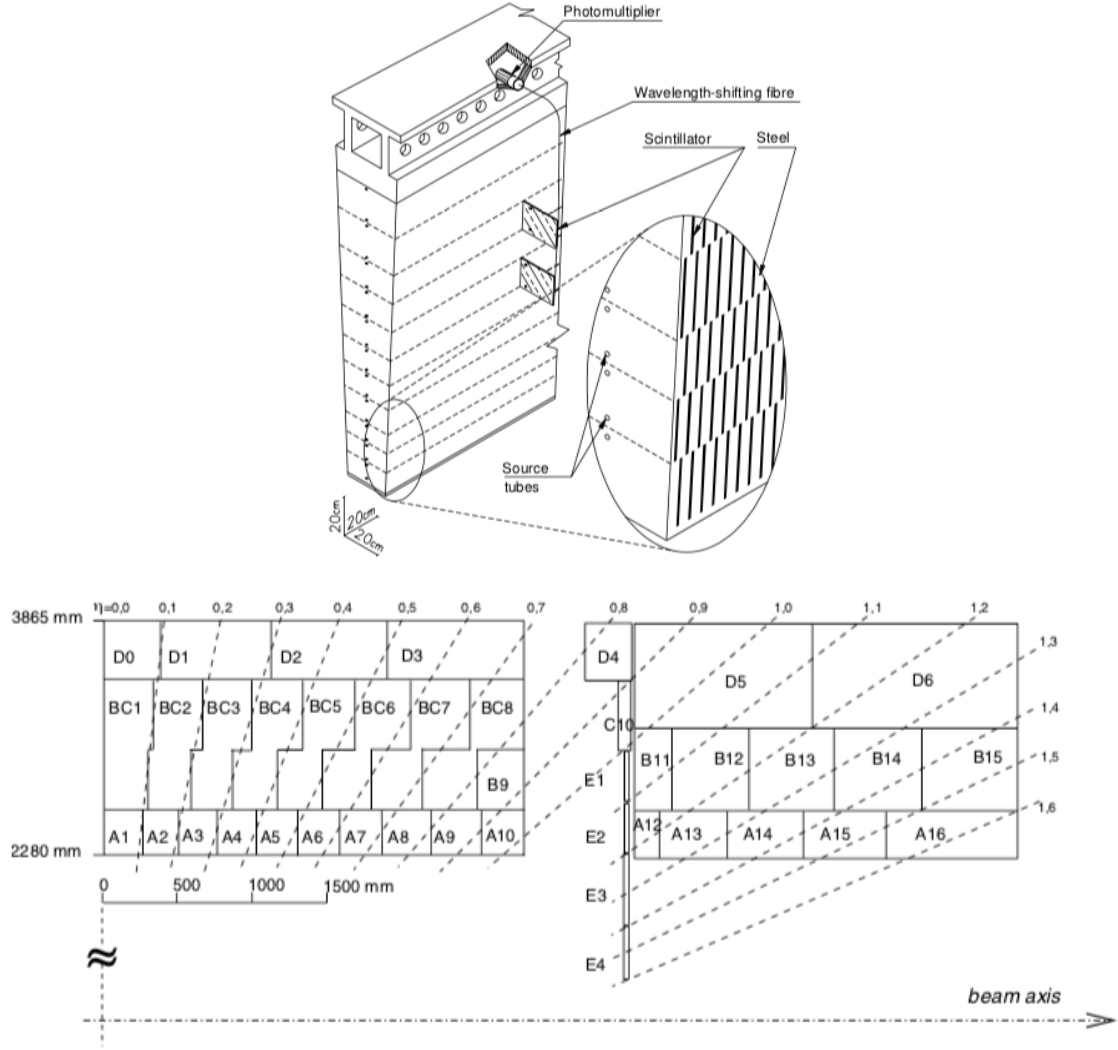


Figure 1.17: *Top:* A view of a tile calorimeter module with its interleaved steel absorbers and scintillating tiles and PMT readout. Also indicated are the source tubes through which radioactive Cesium (Cs) sources are passed for calibration purposes [23]. *Bottom:* Illustration of the segmentation of the projective readout of both the barrel and extended barrel tile calorimeter.

## Forward Calorimeter

The forward calorimeter (FCal) system [24] provides calorimetric coverage to high  $|\eta|$ , between  $3.1 < |\eta| < 4.9$ , furthering the hermeticity of the detector. As indicated in Figure 1.18, FCal consists of three layers in the  $z$  direction: an electromagnetic layer (FCal 1) and two hadronic layers (FCal 2 and FCal 3). All three layers use LAr as the active medium but differ in their passive media. FCal 1 uses copper for its absorber, chosen for its heat removal properties, while FCal 2 and FCal 3 use tungsten, chosen to provide high containment and minimisation of the lateral spread of hadronic showers. The FCal modules consist of matrices of the passive material with regularly spaced readout tubes oriented parallel to the beam-pipe that are filled with the cooled LAr.

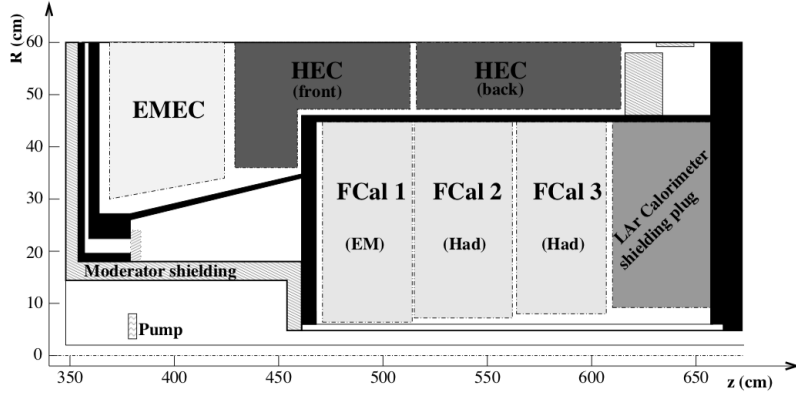


Figure 1.18: View of the forward calorimeter (FCal) system. Portions of the electromagnetic and hadronic end-cap systems are also shown.

### 1.2.4 The Muon Spectrometer

Surrounding the calorimeters is the muon spectrometer (MS) [25], responsible for the detection of high-momentum, minimum-ionizing muons originating from the  $pp$  interaction. The MS is based on the magnetic deflection of muon tracks, allowing for their momentum determination. The bending of the muon trajectories is provided by the large superconducting air-core toroid magnet system, illustrated in Figure 1.10, consisting of a large barrel toroid over the range  $|\eta| < 1.4$  and end-cap toroid systems in the range  $1.6 < |\eta| < 2.7$ . The superconducting toroid magnet provides an average field of 4 T. The magnetic field bending strength is roughly constant in  $\eta$ , except in the region in which the transition between the barrel and end-cap toroids takes place ( $1.4 < |\eta| < 1.6$ ). A view of the ATLAS detector is shown in Figure 1.19, where it can be seen that the volume enclosed by the MS takes up most of the available volume outside of the calorimeter systems in the underground experimental cavern at Point 1. It should be noted that the overall design of the superconducting toroid structure, dictated by the performance requirements of the MS, is what gives ATLAS its large size and essentially drove the original design of all subdetectors discussed in

the previous sections.

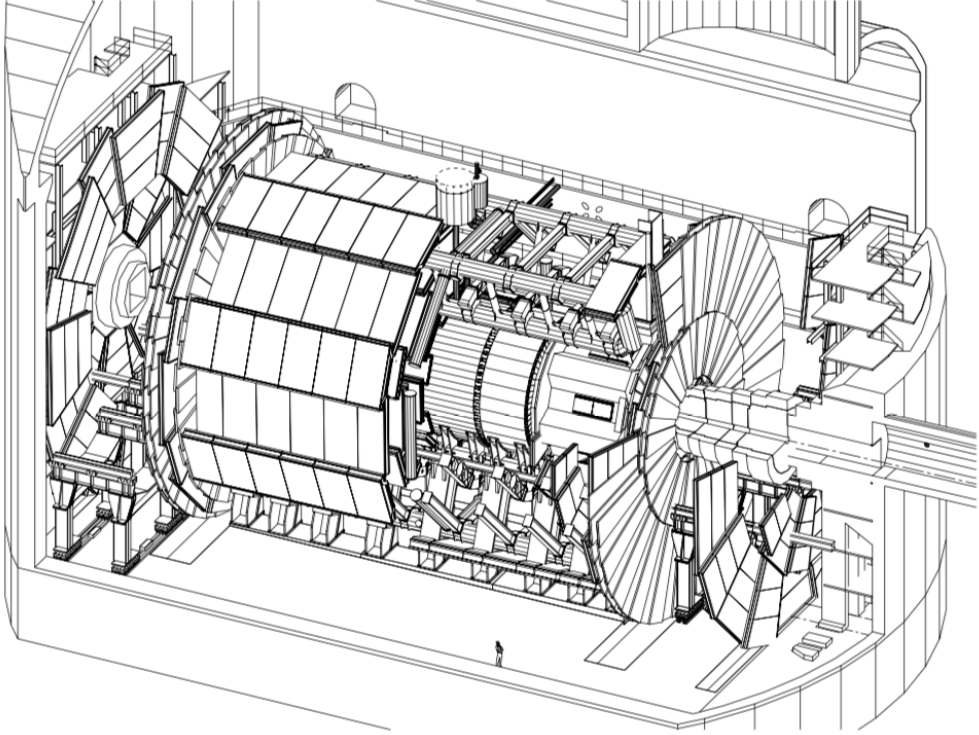


Figure 1.19: A view of the ATLAS detector inside the underground experimental area UX15. The cut-away view exposes the toroid structure as well as the calorimeter system. Notice that the outermost muon stations in the forward regions are located at the extreme ends of the cavern.  
**Should move this figure either above or entirely**

There are four types of gaseous radiation detector used in the MS, and their chamber layout is based on the concept of projective towers. The chambers follow the structure of the toroid magnet structure and have a 16-fold segmentation in azimuth, shown in Figure 1.20. They are arranged in large and small sectors, with the large sectors covering the regions between the coils of the toroid and the small sectors the azimuthal range in which the coils sit. The detector types can be broken into two classes and are either *precision* or *trigger* chambers. The precision chambers are composed of Monitored Drift Tube (MDT) and Cathode Strip Chamber (CSC) detectors and allow for the precise measurement the muon tracks as they traverse the MS, specifically the precise measurement in the bending plane of these tracks so as to allow for accurate determination of the muon momenta through their curvature. The trigger chambers are composed of Resistive Plate Chamber (RPC) and Thin Gap Chamber (TGC) detectors and have fast signal formation and readout times, allowing for accurate assignment of a passing muon to a specific  $pp$  bunch crossing. Both types of detectors exist in the barrel and end-cap *stations* of the MS and there are typically at least three layers of precision-type chambers over the entire  $|\eta|$  range of the MS in order to allow for the sagitta measurement of the muon tracks necessary for momentum determination. The

number of precision chamber hits over the entire range in  $\eta - \phi$  of the MS is shown on the left side of Figure 1.21. In the regions  $|\eta| \sim 0$  and  $|\eta| \sim 1.2$  there are noticeable drops in chamber coverage in order to allow for ID and calorimeter services and in the transition region between the barrel and end-cap, respectively, as seen on the right side of Figure 1.21.

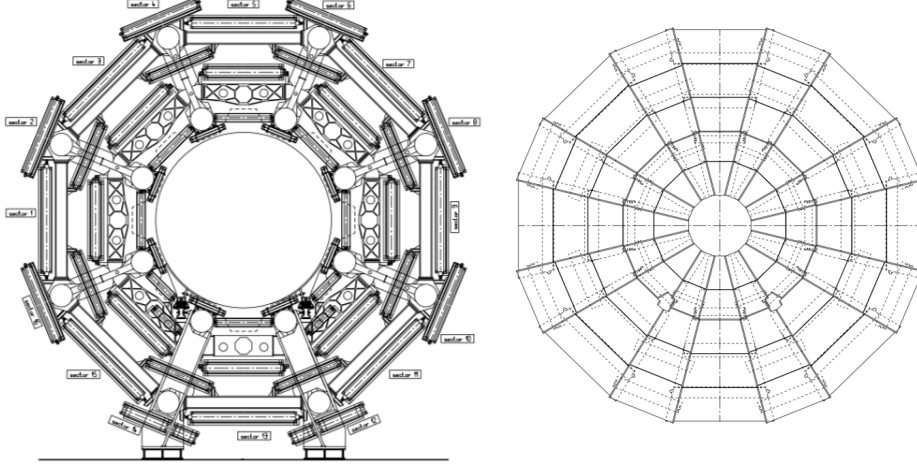


Figure 1.20: View of the 16-fold segmentation of the muon spectrometer in the barrel (*left*) and end-cap (*right*). Clearly seen in both is the arrangement of the detector chambers into large and small sectors, allowing for complete coverage in azimuth. The view of the end-cap is that only of the MDT chambers located at  $z \approx 13$  m.

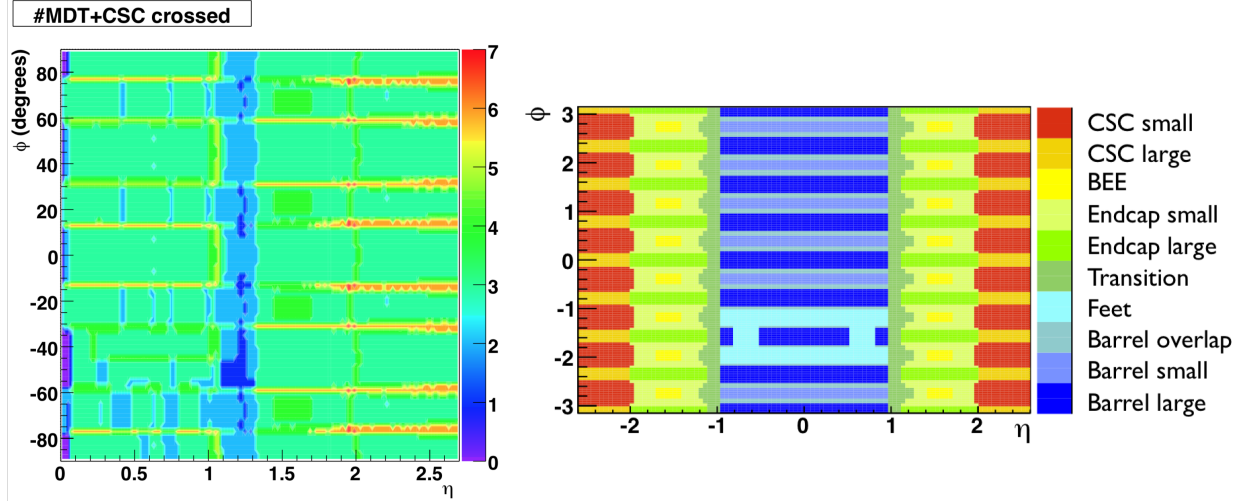


Figure 1.21: *Left:* Number of precision muon chambers (MDT and CSC) traversed by a muon passing through the muon spectrometer as a function of  $\eta$  and  $\phi$ . The regions of high numbers of crossings ( $> 4$ ) correspond to the regions of overlap between the large and small sectors. *Right:* Location in  $\eta - \phi$  of several regions of the MS.

The layout of the muon chambers and the corresponding detector technologies in the barrel and

end-cap sections shown in Figure 1.22. Here we will briefly describe each, starting with the barrel section

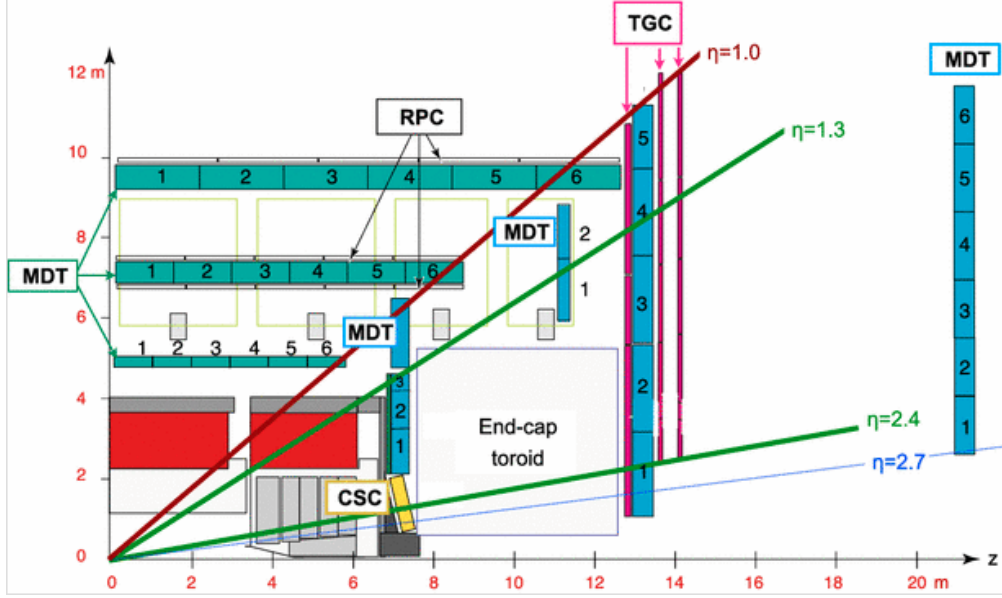


Figure 1.22: A view in the  $r - z$  plane of a quadrant of the muon spectrometer (MS). Indicated by color are the four detector technologies used in the MS: MDT (blue), RPC (grey), TGC (red), and CSC (yellow). The light grey boxes at  $6 < r < 9$  m indicate the location of the barrel toroid structures. Also shown are the envelopes in  $|\eta|$  of the barrel, small wheel, and big wheel sections of the MS.

### Muon Spectrometer: Barrel

The muon chambers in the barrel section of the MS are rectangular in shape and arranged in 3 cylindrical shells, concentric about and parallel to the beam-axis at radial distances of 5, 7.5, and 10.5 m (see Figure 1.20). The precision chambers in the barrel section are composed of MDT chambers with tubes perpendicular to the beam-axis and parallel to the toroidal magnetic field, allowing for precision measurement along  $\eta$ . The MDT tubes are 3 cm in diameter and contain a 93% Ar – 7% CO<sub>2</sub> gas mixture with a single tungsten-rhenium wire operated at 3 kV. Traversal of a minimum ionising particle (MIP) ionises the gas within the tube, and the signal of the resulting ionisation charge is readout. The typical spatial resolution of a single MDT tube is below 100  $\mu\text{m}$ . The MDT chambers are built as multi-layers of many MDT tubes which allows for the improvement of the spatial resolution down to 50  $\mu\text{m}$ . An MDT double multi-layer chamber is shown in Figure 1.23. Also illustrated in this figure is the principle by which the tube hits in a given MDT multi-layer are used to form tracklets which aid in the determination of the muon track building.

The chambers responsible for constructing muon trigger primitives in the MS barrel are the RPC chambers, whose principle of operation is shown on the left of Figure 1.25. The RPC gap is

2 mm, filled with tetrafluorethane ( $C_2H_2F_4$ ), and is lined with parallel plate electrodes operated at a potential difference of 9.8 kV. This high operating potential and gas mixture allows for a timing resolution of 2 ns. Readout strips in  $x$  and  $y$  collect the induced charge from the ionisation events within the gap and provide additional spatial information for track building.

### Muon Spectrometer: End-cap

#### Precision Muon Chambers

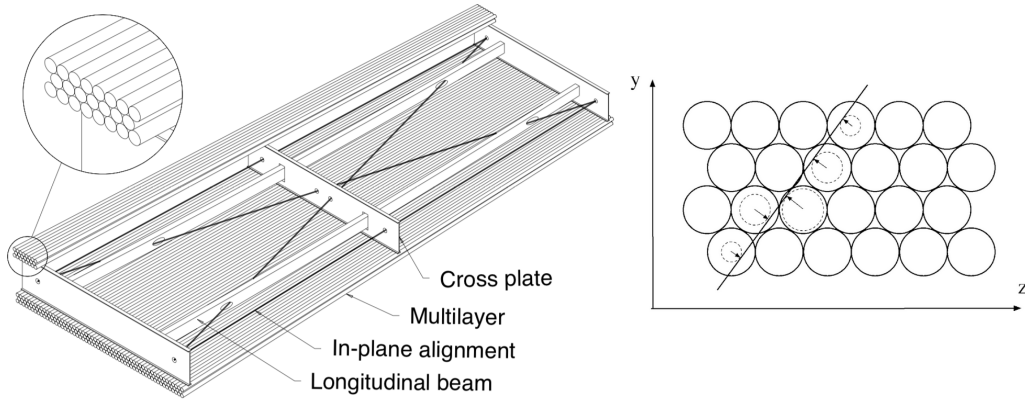


Figure 1.23: *Left:* Illustration of a double-multilayer MDT chamber with its internal alignment and support structure exposed. A zoom-in on the multilayer of MDT tubes is shown. *Right:* Illustration of the multilayer MDT tracklet-fitting algorithm [26].

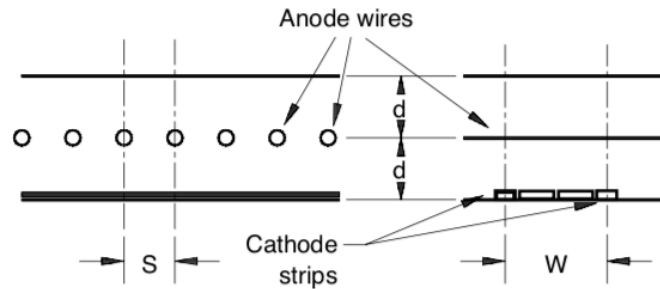


Figure 1.24: Diagram showing the main components of a cathode-strip chamber (CSC). On the *left* (*right*) is a view parallel (perpendicular) to the anode wires and perpendicular (parallel) to the cathode strips.

### Muon Trigger Chambers

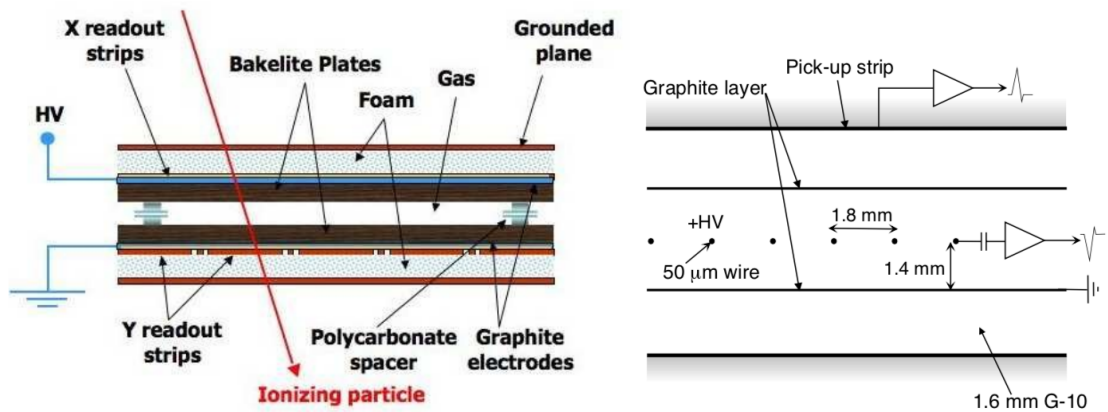


Figure 1.25: Muon trigger chambers. *Left:* Illustration of a resistive plate chamber (RPC) and its principle of operation. *Right:* Diagram showing the main components of a thin-gap chamber (TGC).

# Bibliography

- [1] “CERN Annual Personnel Statistics 2018”. In: (2018). URL: <https://cds.cern.ch/record/2677223> (cit. on p. 1).
- [2] The ALICE Collaboration. “The ALICE experiment at the CERN LHC”. In: *Journal of Instrumentation* 3.08 (Aug. 2008), S08002–S08002. DOI: [10.1088/1748-0221/3/08/s08002](https://doi.org/10.1088/1748-0221/3/08/s08002). URL: <https://doi.org/10.1088%2F1748-0221%2F3%2F08%2Fs08002> (cit. on p. 1).
- [3] The LHCb Collaboration. “The LHCb Detector at the LHC”. In: *Journal of Instrumentation* 3.08 (Aug. 2008), S08005–S08005. DOI: [10.1088/1748-0221/3/08/s08005](https://doi.org/10.1088/1748-0221/3/08/s08005). URL: <https://doi.org/10.1088%2F1748-0221%2F3%2F08%2Fs08005> (cit. on p. 1).
- [4] The CMS Collaboration. “The CMS experiment at the CERN LHC”. In: *Journal of Instrumentation* 3.08 (Aug. 2008), S08004–S08004. DOI: [10.1088/1748-0221/3/08/s08004](https://doi.org/10.1088/1748-0221/3/08/s08004). URL: <https://doi.org/10.1088%2F1748-0221%2F3%2F08%2Fs08004> (cit. on p. 1).
- [5] The ATLAS Collaboration. “The ATLAS Experiment at the CERN Large Hadron Collider”. In: *Journal of Instrumentation* 3.08 (Aug. 2008), S08003–S08003. DOI: [10.1088/1748-0221/3/08/s08003](https://doi.org/10.1088/1748-0221/3/08/s08003). URL: <https://doi.org/10.1088%2F1748-0221%2F3%2F08%2Fs08003> (cit. on pp. 1, 17).
- [6] Lyndon Evans and Philip Bryant. “LHC Machine”. In: *Journal of Instrumentation* 3.08 (Aug. 2008), S08001–S08001. DOI: [10.1088/1748-0221/3/08/s08001](https://doi.org/10.1088/1748-0221/3/08/s08001). URL: <https://doi.org/10.1088%2F1748-0221%2F3%2F08%2Fs08001> (cit. on pp. 2, 7).
- [7] *LEP Design Report: Vol. 1: The LEP Injector Chain*. CERN, 1983. URL: <https://cds.cern.ch/record/98881> (cit. on p. 3).
- [8] *LEP Design Report: Vol. 2: The LEP Main Ring*. CERN, 1984. URL: <https://cds.cern.ch/record/102083> (cit. on p. 3).
- [9] Stephen Holmes, Ronald S Moore, and Vladimir Shiltsev. “Overview of the Tevatron collider complex: goals, operations and performance”. In: *Journal of Instrumentation* 6.08 (Aug. 2011), T08001–T08001. DOI: [10.1088/1748-0221/6/08/t08001](https://doi.org/10.1088/1748-0221/6/08/t08001). URL: <https://doi.org/10.1088%2F1748-0221%2F6%2F08%2Ft08001> (cit. on p. 3).
- [10] Juan Casas et al. “Design concept and first experimental validation of the superfluid helium system for the large hadron collider (LHC) project at CERN”. In: *Cryogenics* 32 (1992), pp. 118–121. DOI: [10.1016/0011-2275\(92\)90122-Q](https://doi.org/10.1016/0011-2275(92)90122-Q) (cit. on p. 4).

- [11] *ECFA-CERN Workshop on Large Hadron Collider in the LEP tunnel*. CERN. Geneva: CERN, 1984. DOI: 10.5170/CERN-1984-010-V-1. URL: <https://cds.cern.ch/record/154938> (cit. on p. 5).
- [12] Oliver Sim Brüning et al. *LHC Design Report: Vol. 1: The LHC Main Ring*. CERN Yellow Reports: Monographs. Geneva: CERN, 2004. DOI: 10.5170/CERN-2004-003-V-1. URL: <https://cds.cern.ch/record/782076> (cit. on p. 6).
- [13] Oliver Sim Brüning et al. *LHC Design Report: Vol. 2: The LHC Infrastructure and General Services*. CERN Yellow Reports: Monographs. Geneva: CERN, 2004. DOI: 10.5170/CERN-2004-003-V-2. URL: <https://cds.cern.ch/record/815187> (cit. on p. 8).
- [14] Michael Benedikt et al. *LHC Design Report: Vol. 3: The LHC Injector Chain*. CERN Yellow Reports: Monographs. Geneva: CERN, 2004. DOI: 10.5170/CERN-2004-003-V-3. URL: <https://cds.cern.ch/record/823808> (cit. on pp. 6, 10).
- [15] R Scrivens et al. “Overview of the status and developments on primary ion sources at CERN\*”. In: CERN-ATS-2011-172 (Sept. 2011), 4 p. URL: <https://cds.cern.ch/record/1382102> (cit. on p. 7).
- [16] Daniel Boussard and Trevor Paul R Linnecar. *The LHC Superconducting RF System*. Tech. rep. LHC-Project-Report-316. CERN-LHC-Project-Report-316. Geneva: CERN, Dec. 1999. URL: <https://cds.cern.ch/record/410377> (cit. on p. 8).
- [17] Werner Herr and B Muratori. “Concept of luminosity”. In: (2006). DOI: 10.5170/CERN-2006-002.361. URL: <https://cds.cern.ch/record/941318> (cit. on p. 10).
- [18] S Haywood et al. “ATLAS inner detector: Technical Design Report, 2”. In: Technical Design Report ATLAS (1997). URL: <http://cds.cern.ch/record/331064> (cit. on p. 14).
- [19] M Capeans et al. *ATLAS Insertable B-Layer Technical Design Report*. Tech. rep. CERN-LHCC-2010-013. ATLAS-TDR-19. Sept. 2010. URL: <https://cds.cern.ch/record/1291633> (cit. on p. 15).
- [20] M. Backhaus. “The upgraded Pixel Detector of the ATLAS Experiment for Run 2 at the Large Hadron Collider”. In: *Nucl. Instrum. Meth.* A831 (2016), pp. 65–70. DOI: 10.1016/j.nima.2016.05.018 (cit. on p. 17).
- [21] *ATLAS liquid-argon calorimeter: Technical Design Report*. Technical Design Report ATLAS. Geneva: CERN, 1996. URL: <https://cds.cern.ch/record/331061> (cit. on p. 18).
- [22] *ATLAS tile calorimeter: Technical Design Report*. Technical Design Report ATLAS. Geneva: CERN, 1996. URL: <https://cds.cern.ch/record/331062> (cit. on p. 18).
- [23] Marija Marjanovic. “ATLAS Tile calorimeter calibration and monitoring systems”. In: *21st IEEE Real Time Conference (RT2018) Williamsburg, Virginia, June 11-15, 2018*. 2018. arXiv: 1806.09156 [physics.ins-det] (cit. on p. 21).

- [24] A Artamonov et al. “The ATLAS Forward Calorimeter”. In: *Journal of Instrumentation* 3.02 (Feb. 2008), P02010–P02010. doi: 10.1088/1748-0221/3/02/p02010. URL: <https://doi.org/10.1088%2F1748-0221%2F3%2F02%2Fp02010> (cit. on p. 22).
- [25] *ATLAS muon spectrometer: Technical Design Report*. Technical Design Report ATLAS. Geneva: CERN, 1997. URL: <https://cds.cern.ch/record/331068> (cit. on p. 22).
- [26] P Branchini et al. “Global Time Fit for Tracking in an Array of Drift Cells: The Drift Tubes of the ATLAS Experiment”. In: *Nuclear Science, IEEE Transactions on* 55 (Mar. 2008), pp. 620–627. doi: 10.1109/TNS.2007.914020 (cit. on p. 26).